SUPPORTING INFORMATION

Correlated Fluctuations and Intraband Dynamics of J-Aggregates Revealed by Combination of 2DES Schemes

Luca Bolzonello,[†] Francesca Fassioli,[*,‡] and Elisabetta Collini[*,†]

†*Department of Chemical Sciences, University of Padova, Via Marzolo 1, Padova*

‡*Department of Physics, University of Trieste, Strada Costiera 11, Trieste*

E-mail: Francesca.Fassioli@ts.infn.it; elisabetta.collini@unipd.it

S1 Energy spectrum and optical transitions in a molecular chain

We consider an aggregate of N molecules electronically coupled. Restricting the dynamics to a maximum of 2-excitations, the Hamiltonian describing the purely electronic degrees of freedom can be written as

$$H_{el} = H_{el}^{(0)} + H_{el}^{(1exc)} + H_{el}^{(2exc)} \tag{S.1}$$

$$\tag{S.2}$$

where $H_{el}^{(0)}$, $H_{el}^{(1exc)}$ and $H_{el}^{(2exc)}$ stand for the ground, single-exciton and two-exciton Hamiltonian respectively and are given by

$$H_{el}^{(0)} = e_0|0\rangle\langle 0| \tag{S.3}$$

$$H_{el}^{(1exc)} = \sum_{m}^{N} e_m|m\rangle\langle m| + \sum_{n>m}^{N} J_{mn}|m\rangle\langle n| \tag{S.4}$$

$$H_{el}^{(2exc)} = \sum_{m=1}^{N}\sum_{n>m}^{N}(e_m + e_n)|mn\rangle\langle mn| + J_{mn}(\sum_{k\neq m,n}^{N}|mk\rangle\langle nk| + h.c.). \tag{S.5}$$

$|0\rangle$ denotes the state with all molecules in the ground electronic state, $\{|m\rangle\}$ are the single-exciton states denoting the state with molecule m excited and all others in the ground state and $\{|mn\rangle\}$ are the two-exciton states that represent the states with molecules m and n excited and all others in the ground state. For the case of an homogeneous linear chain $e_m \equiv E$ with nearest neighbour coupling $J_{mn} \equiv J(\delta_{m,n+1} + \delta_{m,n-1})$, the energy spectrum in the single-exciton subspace of $H_{el}^{(1exc)}$ is given by (F.C. Spano et al, *Phys. Rev. Lett.*, **1991**, 67, 3424)

$$E_k \;=\; E + 2J\cos\Big(\frac{\pi k}{N+1}\Big),\; k = 1 \ldots N \tag{S.6}$$

Assuming equal transition dipole moments for each molecule such that $\mu = \sum_m \mu_m |\Psi_m(g)\rangle\langle\Psi_m(e)| + h.c.$) with $\Psi_m(g(e))$ the ground (first-excited) electronic state of molecule m, optical transitions in the aggregate are only allowed to eigenstates with odd k numbers and the transition dipole strength rapidly decreases with k, such that most of the oscillator strength is carried by the $k = 1$ transition. The eigenenergies of the two-exciton Hamiltonian $H_{el}^{(2exc)}$ are given by $E_{k,k'} = E_k + E_{k'}$ with $k \neq k' = 1 \ldots N$. The strongest dipole transition from the $k = 1$ single-exciton state is to the lowest two-exciton state $k, k' = 1, 2$ with energy $E_1 + E_2$. Notice then that the excited-state absorption happens at an energy which is lower than the sum of the two lowest optically bright single-exciton states $E_1 + E_3$.

Estimation of single-exciton energy gaps: From Eq. S.6 we can relate the single-exciton energy gaps with J and N as

$$E_k - E_{k'} = 2J\Big\{\cos\Big(\frac{\pi k}{N+1}\Big) - \cos\Big(\frac{\pi k'}{N+1}\Big)\Big\}. \tag{S.7}$$

The above model applies to a purely electronic system. In real aggregates, coupling to vibrations will give rise to vibronic states of mixed vibrational and electronic origin. However if the vibronic coupling is weak and there are no particular resonant conditions between exciton gaps and vibrational frequencies, as in our case (see model and parameters below), the vibronic coupling will only weakly mix different exciton states and the vibronic states will have predominantly a single k electronic character, with the strongest transitions having energies close to those of the excitonic system. Under this condition, we are allowed, as described in the main text, to estimate the $E_2 - E_1 \sim \Delta_{\omega_3} \approx 180$ cm^{-1} exciton gap through the 2Q2D experiment, which allows us in turn, through Eq. S.7, to estimate the electronic

coupling J as a function of the total number of molecules over which the excitation delocalizes N. Using again Eq. S.7 we can obtain all other single-exciton energy gaps, and in particular $E_3 - E_1$, as a function of N. Since the approximate value of E_1 is also known (through the linear spectra and conventional 2DES experiments), this leads to the estimate of the monomer energy E as a function of N (Eq. S.6). The monomer transition energy should be close to the maximum in the absorption of the monomer (at ≈ 23800 cm^{-1}) which allows us to estimate the value of N and therefore also E_3. An exciton gap in the range of $E_2 - E_1 \approx$ 160-200 cm^{-1} leads to $J \approx -(1170\text{-}1400)$ cm^{-1}, $N \approx$ 12-14 monomers and $E_3 - E_1 \approx$ 416-520 cm^{-1}. This is consistent with assigning the frequency of 445 cm^{-1} found in the conventional 2D measures to the 1-3 coherence.

S2 Minimal model and decoherence

S2.1 Minimal Model

We are interested in understanding the vibrational, electronic and possibly vibronic features in the spectra of the J-aggregate. Since calculating the 2D spectra for an aggregate of $N \approx 12$ molecules each coupled to two vibrational modes (or even if only 2 effective modes are considered) is very demanding computationally, we use a minimal model that involves the most probable optical transitions in the system. We consider a four level electronic system, consisting of the ground state $|0\rangle$, the $k = 1$, $|1\rangle$ and $k = 3$, $|3\rangle$ exciton states, and the lowest two-exciton state with $k, k' = 1, 2$, $|1, 2\rangle$. The vibronic coupling in this minimal model is included by considering the coupling of the electronic states to two effective vibrational modes. The total Hamiltonian for the system is written as

$$H_s = H_{el} + H_{el,vib} + H_{vib}. \tag{S.8}$$

The electronic, electronic-vibrational (vibronic) coupling and vibrational Hamiltonians are given by

$$H_{el} = E_1|1\rangle\langle 1| + E_3|3\rangle\langle 3| + E_{12}|1,2\rangle\langle 1,2| \quad \text{(S.9)}$$

$$H_{el,vib} = \sum_{i=\alpha,\beta} g_i(a_i^\dagger + a_i)(|1\rangle\langle 3| + |3\rangle\langle 1|)$$

$$H_{vib} = \hbar\omega_\alpha a_\alpha^\dagger a_\alpha + \hbar\omega_\beta a_\beta^\dagger a_\beta. \quad \text{(S.10)}$$

The operators $a_{\alpha(\beta)}^\dagger$ and $a_{\alpha(\beta)}$ denote the creation and annihilation operators of phonon modes respectively and $\omega_{\alpha(\beta)}$ is the vibrational frequency. The vibronic coupling will give rise to vibronic states in the single-exciton subspace with energies that will be a function of $E_{1(3)}$, g_i and ω_i. In particular, the g parameter in our model is related to an effective Huang-Rhys factor S by $g = \omega_{vib}\sqrt{S}$, where S is expected to be reduced with respect to the molecular Huang-Rhys factor due to exciton delocalization (J. Lim et al, *Nat. Commun.* **2015**, 6, 7755).

S2.2 Decoherence

We assume that the electronic transitions couple weakly to a thermal bath in equilibrium such that decoherence due to the bath is modeled by a Markovian dissipator $\mathcal{D}_{el}$ obtained within the Born-Markov and rotating wave (secular) approximations (H.-P. Breuer and F. Petruccione, *The Theory of Open Quantum Systems* **2002**, Oxford University Press: New York).

Before going into the full decoherence model used in our calculations, we first illustrate the effect of correlated fluctuations in exciton dephasing, which we will show to be relevant in our system. For this, we write the microscopic form of the terms in the dissipator that lead to dephasing in the single and one-exciton manifolds (F. Fassioli et al, *J. Phys. Chem. Lett.* **2010**, 1, 2139-2143):

$$\mathcal{D}_{el}^{(1)} = \sum_{m,m'=1}^{N} \sum_{\omega} \gamma_{mm'}(\omega)(A_{m'}(\omega)\rho(t)A_m^\dagger(\omega) - \frac{1}{2}\{A_m^\dagger(\omega)A_{m'}(\omega), \rho(t)\}). \quad \text{(S.11)}$$

m and m' label all molecular sites while $\omega = E_{K'} - E_K \equiv \omega_{K'K}$ labels all possible single-exciton energy differences with K, K' denoting exciton states. $A_m(\omega) = \langle m|K\rangle\langle K'|m\rangle|K\rangle\langle K'|$ for $\omega \neq 0$ and $A_m(0) = \sum_K |c_m(K)|^2|K\rangle\langle K|$ for $\omega = 0$. The operators with $\omega \neq 0$ induce transfer between single exciton states while those associated to $\omega = 0$ induce pure-dephasing. The dissipator $\mathcal{D}_{el}^{(1)}$ induces dephasing between single exciton states K and K' at a rate $\Gamma_{KK'}$ and between the ground state and the one-exciton states at a rate Γ_{0K} given by

$$\begin{aligned}\Gamma_{KK'} &= \sum_{mm'} \gamma_{mm'}(0)(\frac{1}{2}|\langle m|K\rangle|^2|\langle m'|K\rangle|^2 + \frac{1}{2}|\langle m|K'\rangle|^2|\langle m'|K'\rangle|^2 - |\langle m|K'\rangle|^2|\langle m'|K\rangle|^2) \\ &\quad + \sum_{K''} \frac{1}{2}\gamma_{mm'}(\omega_{KK''})\langle m|K''\rangle\langle K|m\rangle\langle K''|m'\rangle\langle m'|K\rangle \\ &\quad + \frac{1}{2}\gamma_{mm'}(\omega_{K'K''})\langle m|K''\rangle\langle K'|M\rangle\langle K''|m'\rangle\langle m'|K'\rangle \end{aligned} \quad \text{(S.12)}$$

$$\begin{aligned}\Gamma_{0K} &= \sum_{mm'} \frac{1}{2}\gamma_{mm'}(0)|\langle m|K\rangle|^2|\langle m'|K\rangle|^2 \\ &\quad + \sum_{K''} \frac{1}{2}\gamma_{mm'}(\omega_{KK''})\langle m|K''\rangle\langle K|m\rangle\langle K''|m'\rangle\langle m'|K\rangle \end{aligned} \quad \text{(S.13)}$$

Notice then that the single exciton dephasing rates are related to the ground-single exciton dephasing rates by

$$\Gamma_{KK'} = \Gamma_{0K} + \Gamma_{0K'} - \sum_{mm'} \gamma_{mm'}(0)|\langle m'|K\rangle|^2|\langle m|K'\rangle|^2 \quad \text{(S.14)}$$

$$= \Gamma_{0K} + \Gamma_{0K'} - \sum_{m} \gamma_{mm}(0)|\langle m|K\rangle|^2|\langle m|K'\rangle|^2 - \sum_{m\neq m'} \gamma_{mm'}(0)|\langle m'|K\rangle|^2|\langle m|K'\rangle|^2 \quad \text{(S.15)}$$

$$\leq \Gamma_{0K} + \Gamma_{0K'} \quad \text{(S.16)}$$

The negative terms on the right hand side of Eq. S.15 have the effect of lowering the single-exciton dephasing rate due to correlated fluctuations between excitons. The first negative term describes correlated fluctuations due to exciton delocalization since it is non-zero as long as the excitons are delocalized over common molecular sites ($|\langle m|K\rangle|^2|\langle m|K'\rangle|^2 \neq 0$). Instead, the second negative term is non-zero as long as the different molecular sites over which the excitons delocalize are under the effect of correlated fluctuations (sites share a common bath: $\gamma_{mm'}(0) \neq 0$ for $m \neq m'$).

For our minimal model we adopt an effective dissipator of Lindblad form where only exciton dephasing (and not population transfer) are included. The dissipator can be recast in the form

$$\begin{aligned}\mathcal{D}_{el} &= \sum_{i=1,3} \Gamma_{0i}(2A_i\rho A_i^\dagger - \{A_i^\dagger A_i, \rho\}) + \gamma_{13}^c(A_1\rho A_3^\dagger + A_3\rho A_1^\dagger) \\ &\quad +\Gamma_{0f}(2A_f\rho A_f^\dagger - \{A_f^\dagger A_f, \rho\}) + \sum_{i=1,3} \gamma_{i,f}^c(A_i\rho A_f^\dagger + A_f\rho A_i^\dagger),\end{aligned} \tag{S.17}$$

where the Lindblad operators are defined as $A_k = |k\rangle\langle k|$. The first and third terms in Eq. S.17 (proportional to Γ_{0i} and Γ_{0f}) induce dephasing between states in the absence of correlations, while the second and last terms (proportional to γ_{13}^c and $\gamma_{i,f}^c$) account for correlated fluctuations of single-exciton states and of single- and the two-exciton states respectively. As explained, correlated dephasing can be due to excitons sharing the same pigments even when the environment-induced fluctuations at each molecule are uncorrelated (local baths: $\gamma_{mm'}(0) \propto \delta_{mm'}$) as well as molecules experiencing correlated fluctuations (shared bath). The exciton coherences evolve due to the dissipator according to

$$\langle 0|\mathcal{D}_{el}|1(3)\rangle = -\Gamma_{01(3)}\langle 0|\rho|1(3)\rangle \quad \text{(S.18)}$$

$$\langle 0|\mathcal{D}_{el}|f\rangle = -\Gamma_{0f}\langle 0|\rho|f\rangle \quad \text{(S.19)}$$

$$\langle 1|\mathcal{D}_{el}|3\rangle = -\Gamma_{13}\langle 1|\rho|3\rangle \quad \text{(S.20)}$$

$$\langle 1(3)|\mathcal{D}_{el}|f\rangle = -\Gamma_{1(3)f}\langle 1(3)|\rho|f\rangle \quad \text{(S.21)}$$

$$\text{(S.22)}$$

where $\Gamma_{13} = \Gamma_{01} + \Gamma_{03} - \gamma^c_{13}$, $\Gamma_{1(3)f} = \Gamma_{01(3)} + \Gamma_{0f} - \gamma^c_{1(3),f}$. As can be seen, the effect of correlated fluctuations is to lower the effective dephasing rate between the single-exciton states $|1\rangle$ and $|3\rangle$ and between the the single exciton $|1(3)\rangle$ and the two-exciton $|f\rangle$ states.

The time evolution of the system's density matrix is dictated by:

$$\frac{d\rho(t)}{dt} = -i[H_s, \rho(t)] + \mathcal{D}_{el}(\rho(t)), \quad \text{(S.23)}$$

which can be expressed in terms of a Liovillian $\mathcal{L}$ that propagates the initial state ρ_0 of the system:

$$\vec{\rho}(t) = e^{\mathcal{L}t}\vec{\rho}_0 \quad \text{(S.24)}$$

where $\vec{\rho}$ is the vectorial representation of the density matrix $\vec{\rho} = \{\rho_{11}, \rho_{12}, \ldots, \rho_{1n}, \rho_{21} \ldots \rho_{nn}\}$.

Parameters: The linear absorption reveals that the absorption maximum of the aggregate is centered around $E_{abs} \approx 20380$ cm^{-1}. 2DES spectra reveals the presence of oscillatory dynamics at frequencies 445 cm^{-1} with a decay time of 265 fs which we ascribe as of predominantly electronic character, and long lived oscillations (> 1 ps) at frequencies of 258 and 334 cm^{-1} which are close to the vibrational frequencies revealed in Raman spectra and which we therefore assign as of predominantly vibrational origin. To incorporate vibrational coherence in our model, we set $\omega_\alpha = 258$ and $\omega_\beta = 334$ cm^{-1} (S.10). We explored a range of weak

to moderate values for the vibronic coupling g_i to fit the dynamics of rephasing and non-rephasing as a function of t_2. We varied $E_{1(3)}$ such that the strongest optical transition from the ground state matched the linear absorption maximum $E_{abs} \approx 20380$ cm^{-1}, and such that the energy gap between the strongest (vibronic state of k1 character) and second strongest (vibronic state of k3 character) optical transition matched 445 cm^{-1}. The best match to experiment was found for $g_\alpha = 0.24\omega_\alpha$ and $g_\beta = 0.2\omega_\beta$ (334 oscillation was less intense than 258 oscillation) which led to a value of $E_1 = 20400$ and $E_3 = 20780$ cm^{-1}. The double-exciton energy is set to $E_{12} = 2E_1 + 170$. To match the linear absorption we set $\Gamma_{01} = 26$ ps^{-1} and $\Gamma_{03} = 40$ ps^{-1} and to match the k1-k3 dephasing time we set $\Gamma_{13} = (0.265ps)^{-1} = 3.8$ ps^{-1}. This dephasing rate is much slower than that predicted for uncorrelated exciton fluctuations $\Gamma_{13} << \Gamma_{01} + \Gamma_{03} = 66$ ps^{-1} suggesting that correlated fluctuations is a fundamental mechanism in such strongly coupled aggregates. The other dephasing rates are set to $\Gamma_{0f} = 40$ ps^{-1}, $\Gamma_{1f} = \Gamma_{01}$ and $\Gamma_{3f} = 2\Gamma_{03}$.

S3 2D spectroscopy

In a non-linear experiment, the radiated signal is proportional to the polarisation of the sample: $\vec{E}_{signal} \propto i\vec{P}$, where the polarisation can be expanded as a sum of the n-th order polarisation $\vec{P} = \sum_n P^n$. The third-order polarization is given by (Bránczyk et al, *Ann. Phys.* **2014** 526, 31-49)

$$\begin{aligned} P^{(3)}(t) &= \left(\frac{i}{\hbar}\right)^3 \int_0^\infty dt_3' \int_0^\infty dt_2' \int_0^\infty dt_1' E(t-t_3')E(t-t_3'-t_2')E(t-t_3'-t_2'-t_1') \times \\ &\quad \mathrm{Tr}\left\{ \Big[[[\mu(t), \mu(t-t_3')], \mu(t-t_3'-t_2')\big], \mu(t-t_3'-t_2'-t_1') \Big] \rho(0) \right\}. \end{aligned} \tag{S.25}$$

We can decompose the electric field by its forward (+) and backward (-) directions of propagation

$$E(t) = \sum_i E_i^+(t) + E_i^-(t) \tag{S.26}$$

where

$$E_i^{\pm}(t) = \epsilon_i(t) e^{\pm i(\vec{k}_i \cdot \vec{r} - \omega_i(t - T_i))}. \tag{S.27}$$

The index i labels all pulses that make up the total electric field that interacts with the system, $\epsilon_i(t)$ is a non-oscillatory function that describes the envelope of the pulse, $\vec{k}_i$ and ω_i are the direction of propagation and the central frequency of the pulse respectively and T_i is the central time of the pulse. The transition dipole moment operator on the other hand, will oscillate with a frequency determined by the optical transitions of the system. For a closed two level system for example, we have that

$$\mu(t) = \mu^-(t)|g\rangle\langle e| + \mu^+(t)|e\rangle\langle g| \tag{S.28}$$

where

$$\mu^{\pm}(t) = \mu e^{\pm i\omega_S t}. \tag{S.29}$$

Products of the type $E_i^{\pm}(t)\mu^{\pm}(t)$ inside the integral in Eq.S.25 will carry a phase $e^{\pm i(-\omega_0+\omega_S)t}$ while products of the type $E_i^{\pm}(t)\mu^{\mp}(t)$ will carry a phase $e^{\mp i(\omega_0+\omega_S)t}$. In an experiment, the central frequency of the pulse ω_i, which we assume equal for all pulses, i.e. $\omega_i \equiv \omega_0$, is typically chosen to be comparable to the characteristic optical transition frequency ω_S of the system under study, $\omega_0 \approx \omega_S$. Therefore, the latter products oscillate very fast and average to zero in the integral Eq.S.25 and can then be safely neglected. Only the $E_i^{\pm}(t)\mu^{\pm}(t)$ products are taken into account. This is known as the rotating wave approximation (RWA). As an example, we notice that due to the RWA, the product $E_i(t - t_3')^- E_{i'}^+(t - t_3' - t_2') E_{i''}^+(t - t_3' - t_2' - t_1')$ will only be multiplied by the product of transition dipole moments given by $\mathrm{Tr}\left\{ \Big[\big[[\mu(t), \mu^-(t - t_3')], \mu^+(t - t_3' - t_2') \big], \mu^+(t - t_3' - t_2' - t_1') \Big] \rho(0) \right\}$.

Due to the fact that $\rho(0)$ does not evolve under the Liouvillian that evolves the operator μ, it can be shown that the time-argument in the transition dipole operators in Eq. S.25 can be shifted by $t_1' + t_2' + t_3' - t$ according to

$$\begin{aligned} \mathrm{Tr}\Big\{ \Big[\big[[\mu(t), \mu(t - t_3')], \mu(t - t_3' - t_2') \big], \mu(t - t_3' - t_2' - t_1') \Big] \rho(0) \Big\} \quad = \\ \mathrm{Tr}\Big\{ \Big[\big[[\mu(t_1' + t_2' + t_3'), \mu(t_2' + t_3')], \mu(t_1') \big], \mu(0) \Big] \rho(0) \Big\}. \end{aligned} \tag{S.30}$$

The third-order polarization Eq. S.25 now reads

$$P^{(3)}(t) \quad = \quad \int_0^\infty dt_3' \int_0^\infty dt_2' \int_0^\infty dt_1' E(t - t_3') E(t - t_3' - t_2') E(t - t_3' - t_2' - t_1') R^{(3)}(t_1', t_2', t_3') \tag{S.31}$$

where the response function R has been defined as

$$R^{(3)}(t_1', t_2', t_3') = \left(\frac{i}{\hbar}\right)^3 \mathrm{Tr}\Big\{ \Big[\big[[\mu(t_1' + t_2' + t_3'), \mu(t_2' + t_3')], \mu(t_1') \big], \mu(0) \Big] \rho(0) \Big\} \tag{S.32}$$

Notice that due to the shift by $t_1' + t_2' + t_3' - t$ in the time-argument in the transition dipole moments, the RWA implies now that only the products involving $E_i^{\pm}(t - t_3')\mu^{\pm}(t_1' + t_2')$, $E_i^{\pm}(t - t_3' - t_2')\mu^{\pm}(t_1')$ and $E_i^{\pm}(t - t_3' - t_2' - t_1')\mu^{\pm}(0)$ survive in the integral Eq.S.31.

In a typical 2DES experiment, the sample interacts with three light pulses that arrive at times T_1, T_2 and T_3. The total electric field is given by the sum of all pulses $E(t) = E_1(t) + E_2(t) + E_3(t)$. If we are interested in the direction of propagation $\vec{k}_s = p_1\vec{k}_1 + p_2\vec{k}_2 + p_3\vec{k}_3$, where $p_i = \pm$, and assuming that all the $\vec{k}_i$ directions are different, the only terms contributing to

the third-order polarization in the RWA are

$$
\begin{aligned}
P^{(3)}_{p_1p_2p_3}(t) &= \int_0^\infty dt'_3 \int_0^\infty dt'_2 \int_0^\infty dt'_1 \times \Big\{ \\
&E_3^{p_3}(t-t'_3)E_2^{p_2}(t-t'_3-t'_2)E_1^{p_1}(t-t'_3-t'_2-t'_1)R^{(3)}_{p_1p_2p_3}(t'_1,t'_2,t'_3) + \\
&E_2^{p_2}(t-t'_3)E_3^{p_3}(t-t'_3-t'_2)E_1^{p_1}(t-t'_3-t'_2-t'_1)R^{(3)}_{p_1p_3p_2}(t'_1,t'_2,t'_3) + \\
&E_3^{p3}(t-t'_3)E_1^{p1}(t-t'_3-t'_2)E_2^{p2}(t-t'_3-t'_2-t'_1)R^{(3)}_{p_2p_1p_3}(t'_1,t'_2,t'_3) + \\
&E_2^{p2}(t-t'_3)E_1^{p1}(t-t'_3-t'_2)E_3^{p3}(t-t'_3-t'_2-t'_1)R^{(3)}_{p_3p_1p_2}(t'_1,t'_2,t'_3) + \\
&E_1^{p1}(t-t'_3)E_2^{p2}(t-t'_3-t'_2)E_3^{p3}(t-t'_3-t'_2-t'_1)R^{(3)}_{p_3p_2p_1}(t'_1,t'_2,t'_3) + \\
&E_1^{p1}(t-t'_3)E_3^{p3}(t-t'_3-t'_2)E_2^{p2}(t-t'_3-t'_2-t'_1)R^{(3)}_{p_2p_3p_1}(t'_1,t'_2,t'_3)\Big\}. \quad \text{(S.33)}
\end{aligned}
$$

with

$$
R^{(3)}_{p_1p_2p_3}(t'_1,t'_2,t'_3) = \left(\frac{i}{\hbar}\right)^3 \mathrm{Tr}\Big\{\Big[\big[[\mu(t'_1+t'_2+t'_3),\mu^{p_3}(t'_2+t'_3)],\mu^{p_2}(t'_1)\big],\mu^{p_1}(0)\Big]\rho(0)\Big\} \quad \text{(S.34)}
$$

If strict time-ordering $T_1 < T_2 < T_3$ is enforced and the light pulses are assumed to be delta-pulses, i.e $E_i(t) = \delta(t - T_i)$, then only the first term in the integral in Eq.S.33 contributes to the third-order polarization and we get

$$
P^{(3)}_{p_1p_2p_3}(t) = \int_0^\infty dt'_3 \int_0^\infty dt'_2 \int_0^\infty dt'_1 E_3^{p_1}(t-t'_3)E_2^{p_2}(t-t'_3-t'_2)E_1^{p_3}(t-t'_3-t'_2-t'_1)R^{(3)}_{p_1p_2p_3}(t'_1,t'_2,t'_3) \quad \text{(S.35)}
$$

$$
= e^{i\vec{k}_S\cdot\vec{r}} R^{(3)}_{p_1p_2p_3}(t_1,t_2,t_3) \quad \text{(S.36)}
$$

where the t_i are the time-delays $t_3 = t - T_3$, $t_2 = T_3 - T_2$ and $t_1 = T_2 - T_1$. As we can see, after the RWA and impulsive limit approximations, the third-order polarization in the $\vec{k}_s = p_1\vec{k}_1 + p_2\vec{k}_2 + p_3\vec{k}_3$ direction is proportional to the response function. Furthermore, the $p_1\vec{k}_1$ direction is associated to the $\pm$ component of the transition dipole moment acting at

$t = 0$, $\mu^{p_1}(0)$, $\vec{p_2} = \pm\vec{k_2}$ is associated to $\mu^{p_2}(t_1)$ and $\vec{p_3} = \pm\vec{k_3}$ is associated to $\mu^{p_3}(t_1 + t_2)$. This leads to the pictorial Feynmann diagram representation of the response function and its relation to the direction of propagation of the signal, where a μ^{p_1} acting at $t = 0$, μ^{p_2} acting at time $t = t_1$ and μ^{p_3} acting at $t = t_1 + t_2$ is associated to the direction of detection $\vec{k}_s = p_1\vec{k}_1 + p_2\vec{k}_2 + p_3\vec{k}_3$. We can see then that if the pulses are not delta pulses and overlap in time, such that other terms besides the first one in the integral Eq. S.33 contribute, the direction of detection will be different than that predicted by the standard Feynmann diagram interpretation. As an example, let's consider the case in which the third term in the integral Eq.S.33, which involves $R^{(3)}_{p_2p_1p_3}$ contributes to the polarization in the $\vec{k}_s = p_1\vec{k}_1 + p_2\vec{k}_2 + p_3\vec{k}_3$ direction. Now p_2 and p_1 are exchanged, so the Feynmann diagram that would be associated to the $\vec{k}_s = p_2\vec{k}_1 + p_1\vec{k}_2 + p_3\vec{k}_3$ direction under the RWA and semi-impulsive limit also contributes. For the polarization in a rephasing experiment $\vec{k}_{reph} = -\vec{k}_1 + \vec{k}_2 + \vec{k}_3$, this means that also terms normally associated to the non-rephasing direction of detection $\vec{k}_{non-reph} = \vec{k}_1 - \vec{k}_2 + \vec{k}_3$ will contribute.

To visualise the 2D spectra in a rephasing or non-rephasing scheme it is convenient to Fourier transform with respect to t_1 and t_3:

$$P^3(\omega_1, t_2, \omega_3) = \int_0^\infty \int_0^\infty dt_1 dt_3 e^{-i\omega_1 t_1} e^{-i\omega_3 t_3} P^3(t_1, t_2, t_3). \tag{S.37}$$

S3.1 Pulse overlap

When light pulses are not close to delta-pulses and overlap in time, the simplified expressions in Eqs.S.35 and S.36 are no longer valid and all possible contributions in Eq.S.33 need to be considered. The polarization in the rephasing direction of detection $\vec{k}_{reph} = -\vec{k}_1 + \vec{k}_2 + \vec{k}_3$ is given by (V. Butkus et al, *Lithuanian Journal of Physics* **2010**, 50, 267-303)

$$
\begin{aligned}
P^{(3)}_{-++}(t) \;=\; & \int_0^\infty dt'_3 \int_0^\infty dt'_2 \int_0^\infty dt'_1 \times \Big\{ \\
& R^{(3)}_{-++}(t'_1,t'_2,t'_3) \times \Big(E^-\big(t_3+t_2+t_1-t'_3-t'_2-t'_1\big) E^+\big(t_3+t_2-t'_3-t'_2\big) E^+\big(t_3-t'_3\big) \\
& + E^-\big(t_3+t_2+t_1-t'_3-t'_2-t'_1\big) E^+\big(t_3+t_2-t'_3\big) E^+ t_3-t'_3-t'_2\big) \Big) \\
& + R^{(3)}_{+-+}(t'_1,t'_2,t'_3) \times \Big(E^-\big(t_3+t_2+t_1-t'_3-t'_2\big) E^+\big(t_3+t_2-t'_3-t'_2-t'_1\big) E^+\big(t_3-t'_3\big) \\
& + E^-\big(t_3+t_2+t_1-t'_3-t'_2\big) E^+\big(t_3+t_2-t'_3\big) E^+\big(t_3-t'_3-t'_2-t'_1\big) \Big) \\
& + R^{(3)}_{++-}(t'_1,t'_2,t'_3) \times \Big(E^-\big(t_3+t_2+t_1-t'_3\big) E^+\big(t_3+t_2-t'_3-t'_2-t'_1\big) E^+\big(t_3-t'_3-t'_2\big) \\
& + E^-\big(t_3+t_2+t_1-t'_3\big) E^+\big(t_3+t_2-t'_3-t'_2\big) E^+\big(t_3-t'_3-t'_2-t'_1\big) \Big) \Big\} \qquad \text{(S.38)}
\end{aligned}
$$

$$
\qquad \text{(S.39)}
$$

The first two terms, are interactions that are associated to the standard (i.e. those relevant under the RWA and semi-impulsive limit) Feynmann diagrams for a rephasing experiment, while the second two terms arise from the interactions normally associated to non-rephasing experiments and the last two terms correspond to contributions associated to 2Q2D experiments.

In the non-rephasing direction $\vec{k}_{reph} = \vec{k}_1 - \vec{k}_2 + \vec{k}_3$

$$
\begin{aligned}
P^{(3)}_{+-+}(t) \;=\; & \int_0^\infty dt'_3 \int_0^\infty dt'_2 \int_0^\infty dt'_1 \times \Big\{ \\
& R^{(3)}_{-++}(t'_1,t'_2,t'_3) \times \Big(E^+\big(t_3+t_2+t_1-t'_3-t'_2\big) E^-\big(t_3+t_2-t'_3-t'_2-t'_1\big) E^+\big(t_3-t'_3\big) \\
& + E^+\big(t_3+t_2+t_1-t'_3\big) E^-\big(t_3+t_2-t'_3-t'_2-t'_1\big) E^+\big(t_3-t'_3-t'_2\big) \Big) \\
& + R^{(3)}_{+-+}(t'_1,t'_2,t'_3) \times \Big(E^+\big(t_3+t_2+t_1-t'_3-t'_2-t'_1\big) E^-\big(t_3+t_2-t'_3-t'_2\big) E^+\big(t_3-t'_3\big) \\
& + E^+\big(t_3+t_2+t_1-t'_3\big) E^-\big(t_3+t_2-t'_3-t'_2\big) E^+\big(t_3-t'_3-t'_2-t'_1\big) \Big) \\
& + R^{(3)}_{++-}(t'_1,t'_2,t'_3) \times \Big(E^+\big(t_3+t_2+t_1-t'_3-t'_2-t'_1\big) E^-\big(t_3+t_2-t'_3\big) E^+\big(t_3-t'_3-t'_2\big) \\
& + E^+\big(t_3+t_2+t_1-t'_3-t'_2\big) E^-\big(t_3+t_2-t'_3\big) E^+\big(t_3-t'_3-t'_2-t'_1\big) \Big) \Big\} \qquad \text{(S.40)}
\end{aligned}
$$

and the 2Q2D direction $\vec{k}_{reph} = \vec{k}_1 + \vec{k}_2 - \vec{k}_3$

$$
\begin{aligned}
P^{(3)}_{++-}(t) &= \int_0^\infty dt'_3 \int_0^\infty dt'_2 \int_0^\infty dt'_1 \times \Big\{ \\
&R^{(3)}_{-++}(t'_1,t'_2,t'_3) \times \Big(E^+(t_3+t_2+t_1-t'_3-t'_2) E^+(t_3+t_2-t'_3) E^-(t_3-t'_3-t'_2-t'_1) \\
&+ E^+(t_3+t_2+t_1-t'_3) E^+(t_3+t_2-t'_3-t'_2) E^- t_3-t'_3-t'_2-t'_1) \Big) \\
&+ R^{(3)}_{+-+}(t'_1,t'_2,t'_3) \times \Big(E^+(t_3+t_2+t_1-t'_3-t'_2-t'_1) E^+(t_3+t_2-t'_3) E^-(t_3-t'_3-t'_2-) \\
&+ E^+(t_3+t_2+t_1-t'_3) E^+(t_3+t_2-t'_3-t'_2-t'_1) E^-(t_3-t'_3-t'_2) \Big) \\
&+ R^{(3)}_{++-}(t'_1,t'_2,t'_3) \times \Big(E^+(t_3+t_2+t_1-t'_3-t'_2-t'_1) E^+(t_3+t_2-t'_3-t'_2) E^-(t_3-t'_3) \\
&+ E^+(t_3+t_2+t_1-t'_3-t'_2) E^+(t_3+t_2-t'_3-t'_2-t'_1) E^-(t_3-t'_3) \Big) \Big\} \qquad \text{(S.41)}
\end{aligned}
$$

The $R^{(3)}_{-++}$ response function is given by

$$
R^{(3)}_{-++}(t'_1,t'_2,t'_3) = R_{-++,2} + R_{-++,3} - R^*_{-++,4} \qquad \text{(S.42)}
$$

where

$$
\begin{aligned}
R_{-++,2}(t'_1,t'_2,t'_3) &= \mathrm{Tr}\Big\{ \mu e^{\mathcal{L}t'_3} \Big(e^{\mathcal{L}t'_2} \big(\mu^+ e^{\mathcal{L}t'_1} (\vec{\rho}_0 \mu^-) \big) \mu^+ \Big) \Big\} & \text{(S.43)} \\
R_{-++,3}(t'_1,t'_2,t'_3) &= \mathrm{Tr}\Big\{ \mu e^{\mathcal{L}t'_3} \Big(\mu^+ e^{\mathcal{L}t'_2} \big(e^{\mathcal{L}t'_1} (\vec{\rho}_0 \mu^-) \mu^+ \big) \Big) \Big\} & \text{(S.44)} \\
R^*_{-++,4}(t'_1,t'_2,t'_3) &= \mathrm{Tr}\Big\{ \mu e^{\mathcal{L}t'_3} \Big(\mu^+ e^{\mathcal{L}t'_2} \mu^+ \big(e^{\mathcal{L}t'_1} (\vec{\rho}_0 \mu^-) \big) \Big) \Big\}. & \text{(S.45)} \\
& & \text{(S.46)}
\end{aligned}
$$

The $R^{(3)}_{+-+}$ response function is given by

$$
R^{(3)}_{+-+}(t'_1,t'_2,t'_3) = R_{+-+,1} + R^*_{+-+,2} - R_{+-+,4} \qquad \text{(S.47)}
$$

where

$$R_{+-+,1}(t_1',t_2',t_3') = \mathrm{Tr}\Big\{\mu e^{\mathcal{L}t_3'}\Big(\mu^+ e^{\mathcal{L}t_2'}\big(\mu^- e^{\mathcal{L}t_1'}(\mu^+\vec{\rho}_0)\big)\Big)\Big\} \tag{S.48}$$

$$R^*_{+-+,2}(t_1',t_2',t_3') = \mathrm{Tr}\Big\{\mu e^{\mathcal{L}t_3'}\Big(\mu^+ e^{\mathcal{L}t_2'}\big(e^{\mathcal{L}t_1'}(\mu^+\vec{\rho}_0)\,\mu^-\big)\Big)\Big\} \tag{S.49}$$

$$R_{+-+,4}(t_1',t_2',t_3') = \mathrm{Tr}\Big\{\mu e^{\mathcal{L}t_3'}\Big(e^{\mathcal{L}t_2'}\big(e^{\mathcal{L}t_1'}(\mu^+\vec{\rho}_0)\,\mu^-\big)\,\mu^+\Big)\Big\}. \tag{S.50}$$

$$\tag{S.51}$$

and finally the $R^{(3)}_{++-}$ contribution is

$$R^{(3)}_{++-}(t_1',t_2',t_3') = R_{++-,1} - R^*_{++-,3} \tag{S.52}$$

where

$$R_{++-,1}(t_1',t_2',t_3') = \mathrm{Tr}\Big\{\mu e^{\mathcal{L}t_3'}\Big(\mu^- e^{\mathcal{L}t_2'}\big(\mu^+ e^{\mathcal{L}t_1'}(\mu^+\vec{\rho}_0)\big)\Big)\Big\} \tag{S.53}$$

$$R^*_{++-,3}(t_1',t_2',t_3') = \mathrm{Tr}\Big\{\mu e^{\mathcal{L}t_3'}\Big(\Big(e^{\mathcal{L}t_2'}\big(\mu^+ e^{\mathcal{L}t_1'}(\mu^+\vec{\rho}_0)\big)\Big)\mu^-\Big)\Big\} \tag{S.54}$$

$$\tag{S.55}$$

To model the electric field, we use assume that the electric field in the frequency domain is real such that $E(t)$ is given by the fourier-transform of the square-root of the experimental spectrum $S(\omega)$ (see Fig. 1 in main text), i.e. $E^-(t) = \int_0^\infty e^{i\omega t}\sqrt{S(\omega)}d\omega$ and $E^+(t) = E^-(t)^*$.

S4 Experimental details

S4.1 Sample preparation and linear characterization

Sample solutions are prepared starting from a water solution of TPPS (PorphyChem) at neutral pH. Sulfuric acid 1 M was added until pH $\approx$ 1.5-2 is reached. The preparation procedure follows the guidelines suggested for the achievement of short linear aggregates

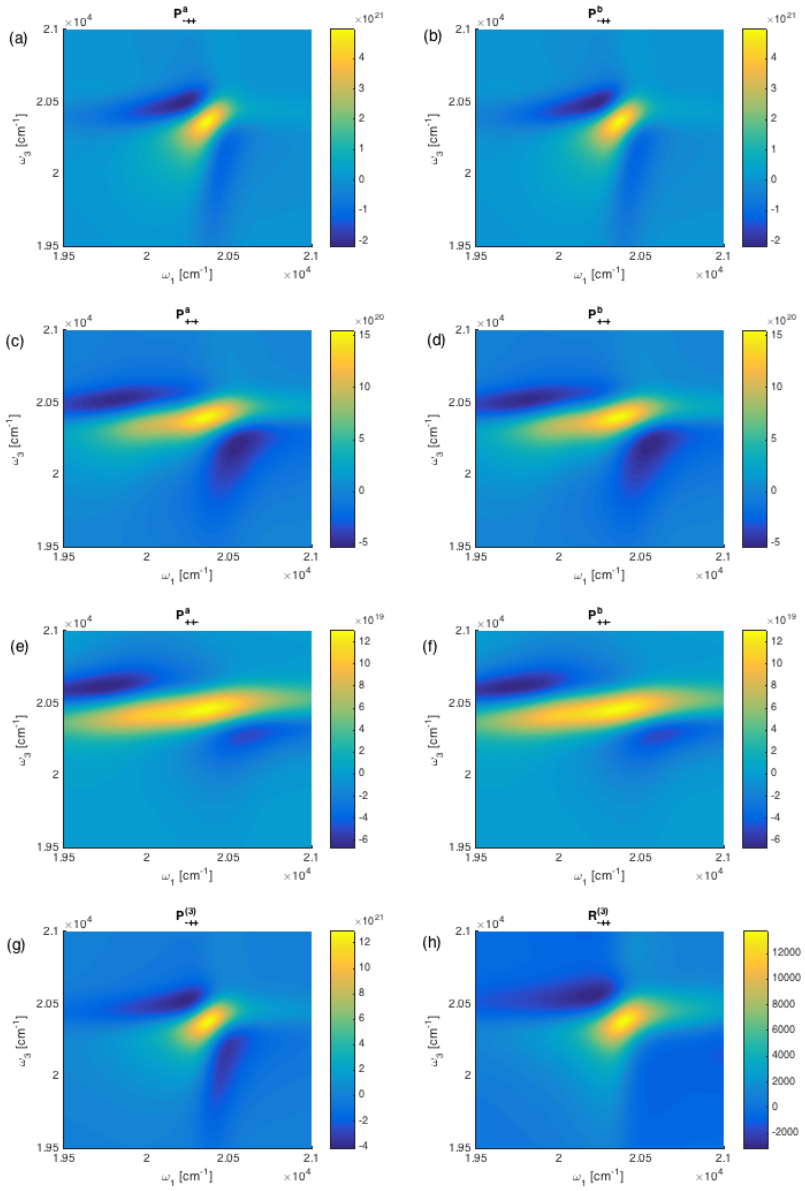

Figure S1: Simulated real rephasing spectra at $t_2 = 0$ (Colorbars in A.U.). (a)-(f) All six contributions to the third-order polarization in the rephasing direction $P^{(3)}_{-++}$ for finite pulse width (Eq. S.39). First (a), second (b), third (c), fourth (d), fifth (e) and sixth (f) term in (Eq. S.39). (g) Total third order polarization $P^{(3)}_{-++} = P^{a}_{-++} + P^{b}_{-++} + P^{a}_{+-+} + P^{b}_{+-+} + P^{a}_{++-} + P^{b}_{++-}$. (h) Impulsive limit spectra $P^{(3)}_{-++} = R^{(3)}_{-++}$. In the impulsive limit the upper negative cross-peak is more intense than the lower negative cross-peak due to excited state absorption ($\omega_1 \sim E_1$, $\omega_3 \sim E_{1,2} - E_1 = E_2$. Finite pulse width effects increase the strength of a negative cross-peak below the diagonal with respect to the impulsive limit scenario.

as stated by Micali et al. (N. Micali et al, *J. Phys. Chem. B*, **2000** 104, 25, 5897-5904). Absorption spectra have been recorded using a Varian Cary 5 spectrophotometer in 1 mm path cells. For 2D experiments the concentration was tuned so to reach absorbance ≈ 0.3 at the excitation wavelength, corresponding to a concentration of about 10 μM of monomeric units.

S4.2 Raman spectroscopy

Raman spectra have been performed with a home-built micro-Raman system, based on a Triax-320 ISA spectrograph, equipped with a holographic 1800 g/mm grating and a CCD detector (Spectrum One ISA Instruments). The excitation source was a Spectra Physics Ar+ laser (Stabilite 2017-06S) operating at 488 and 514 nm for resonant and non-resonant conditions, respectively. A Kaiser Optical System holographic notch filter was used to reduce the stray-light level. An Olympus BX 40 optical microscope equipped with a 20x/0.75 objective was optically coupled to the spectrograph. To avoid optical damage to the sample, the power of the exciting radiation was maintained between 0.15 and 0.5 mW. The Raman spectra were recorded on concentrated solutions (100μM) of H_2TPPS aggregates between 200 and 2000 cm^{-1} and with an instrumental resolution of about 2 cm^{-1} (see figure S2). It was not possible to include in the aggregate solutions an internal standard, therefore the resonant and non-resonant spectra have been normalized on the 1537 cm^{-1} band, as already proposed in the literature (D.L.Akins et al, *J. Phys. Chem.*, **1998** 98, 3612-3618).

S4.3 2D electronic spectroscopy (2DES)

2DES measurements have been performed with a setup similar to the one described in (Nemeth et al, *Opt. Lett.*, **2009**, 34, 3301-3303) and schematized in figure S3 panel a. Briefly, the output of a 800 nm, 3 KHz Ti:Sapphire laser system (Coherent Libra) is converted in a visible broad pulse in an non-collinear optical amplifier (Light Conversion TOPAS White). The transform-limited condition for the pulses at the sample position is achieved through a

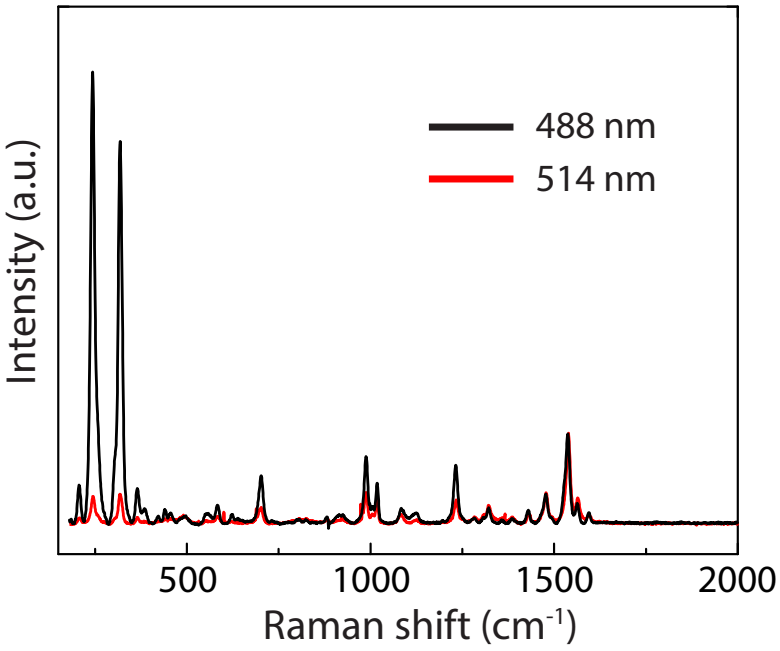

Figure S2: Resonant and non-resonant Raman spectra of concentrated solution of H_2TPPS aggregates in the full range.

prism compressor coupled with a Dazzler pulse shaper for the fine adjustment. The pulse duration is optimized through FROG measures on a solvent using an iterative procedure: the phases of the different wavelength components of the broadband pulse are changed at each iteration until the optimum pulse is obtained. The pulses energy at the sample position is reduced until 5 nJ per pulse by a broadband half-waveplate/polarizer system. The 2DPE experiment relies on the passively phase stabilized setup with a transmission grating already described in the literature (Nemeth et al, *Opt. Lett.*, **2009**, 34, 3301-3303). Briefly, the laser output is splitted into four identical phase-stable beams (three exciting beams and a fourth beam further attenuated of about 3 orders of magnitude used as Local Oscillator, LO) in a BOXCARS geometry using a suitably designed 2D grating. Time delays between pulses are modulated by pairs of 1° fused silica wedges. One glass wedge of each pair is mounted onto a translation stage (Aerotech Ant95), providing a temporal resolution of 0.07 fs. The exciting geometry and time delays definition are illustrated in figure S3 panel b and c.

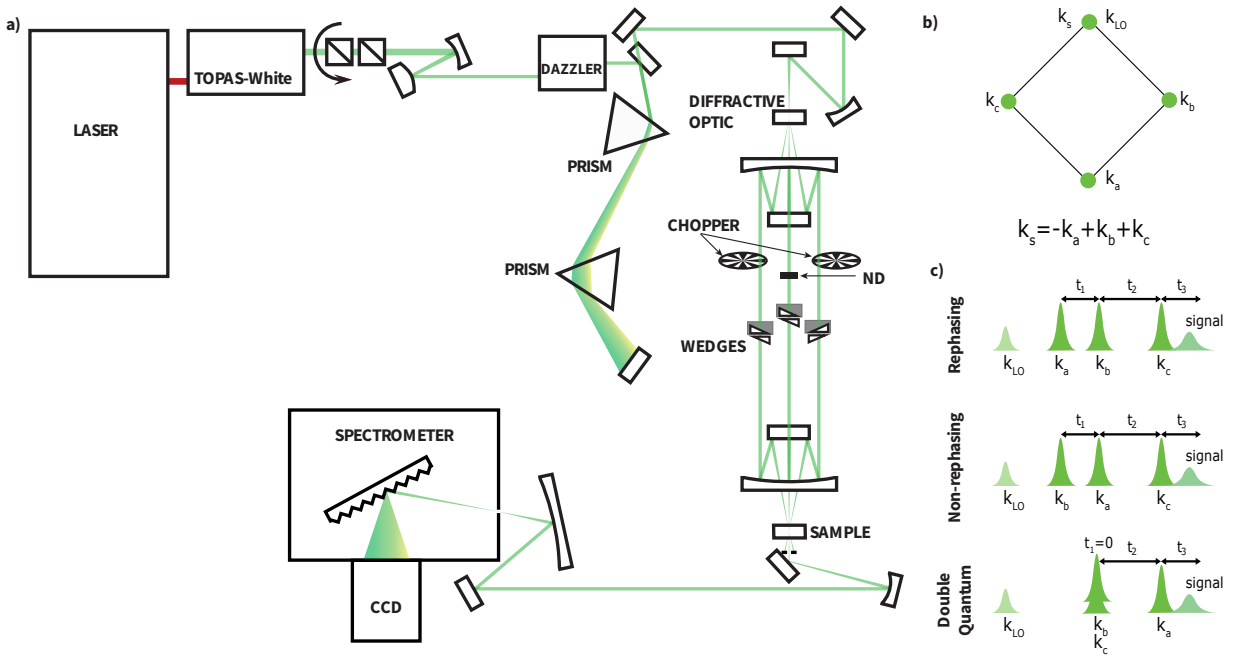

Figure S3: Scheme of the optical setup used for 2D measurements

A digital double lock-in acquisition is implemented (Augulis, R.; Zigmantas D., *Opt. Express* **2011**, 19, 14, 13126-33). Two optical choppers modulate the repetition rate of pulses k_b and k_c at 200 and 40 Hz, respectively. The signal is thus extracted at 160 Hz. The frequency of data collection is set to 500 Hz. This method could remove most of the scattering contributions of the sample.

This setup allows performing different 2D schemes (rephasing (R), non-rephasing (NR) and double quantum (2Q)) through suitable variation of the pulse sequence. The pulse order determines indeed the phase matching conditions (figure S3 panels b, c).

In R and NR measures, for fixed values of t_2, the echo signal is measured while scanning the coherence time t_1, by means of the CCD camera. Thus, the signal evolution over the echo time t_3 is indirectly measured through its Fourier analogue, ω_3. The signal field is thus measured as a function of t_1, t_2, and ω_3. Fourier transformation along t_1 yields finally the signal as a function of ω_1, t_2, and ω_3 , so that the final result is a 2D map in which the signal is plotted as a function of the corresponding coherence frequency ω_1, representing the initial excitation, and the rephasing frequency ω_3, which can be interpreted as the ensuing

emission. To obtain R and NR signals, the relative pulse ordering of beams k_a and k_b is varied as depicted in figure S3 panel c. In our R and NR experiments, t_2 was scanned from 0 to 600 fs in steps of 5 fs and for each value of t_2 the coherence time t_1 was scanned from 0 to 75 fs in steps of 0.32 fs.

In the 2Q experiment instead, t_1 is fixed to 0 while t_2 is scanned. Practically, k_a is kept fixed in time while k_b and k_c are equally delayed. Fourier transformation along t_2 yields the 2Q signal as a function of ω_2, t_1=0, and ω_3 , so that, differently from the R and NR maps, the final 2Q2D map presents the signal as a function of ω_2 and ω_3. The only two Feynman paths contributing to the 2Q signal are shown in figure S4 panel d. The positive contribution (R_4, on the left) and negative contribution (R_3^*, on the right).

In all experiments, the delay between t_3 and t_{LO} is removed so that the signal comes out just after $t_3 = 0$. A supergaussian function with formula $\exp \frac{-(t_3-40fs)^6}{2*(100fs)^6}$ is used as time filter. This function assumes a value ≈ 1 between $t_3 = 0$ and $t_3 = 80$ fs when the signal is present, and quickly decays to 0 beyond this interval where only scattering contribution is collected.

Phasing of R, NR and 2Q spectra follows the procedure described in (Nemeth et al, *Opt. Lett.*, **2009**, 34, 3301-3303) and (Nemeth et al, *J. Chem. Phys.*, **2010**, 133, 094505).

To ensure the reliability of the measures, at least 3 different sets of measures in different days were performed and then averaged. All measurements were performed under ambient temperatures (295 K).

The evolution of the R and NR spectra as a function of t_2 is shown in figure S5.

S4.4 Global fitting analysis

R and NR signals are analyzed with a global complex multi-exponential fit method as proposed in (Volpato, A. et al. *Opt. Express* **2016**, *24*, 24773).

Briefly, the decay of the total complex signal at each point of the 2D map is fitted with a global function written as sum of complex exponentials: $f = \sum_{n=1}^{N} a_n e^{i\phi_n} e^{-t_2/\tau_n} e^{i\omega_n t_2}$. Components with ω_n=0 describe population decay contributions, whereas components with

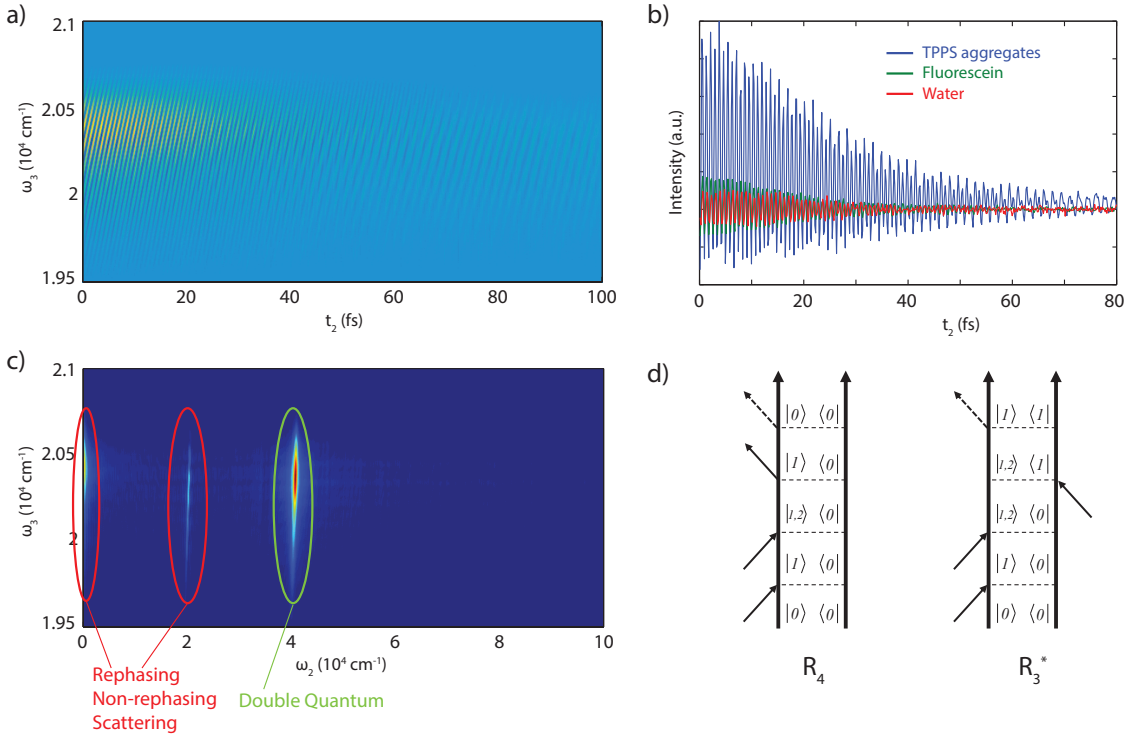

Figure S4: a) 2Q signal as a function of t_2 and ω_3. b) Slice of 2Q signal extracted at $\omega_3 = 20400cm^{-1}$ compared with the same traces extracted from 2Q experiment performed on water and fluorescein solution in the same conditions. The 2Q signal of aggregates is significantly greater because of the resonance with two-exciton states. c) Absolute 2Q signal as a function of ω_2 and ω_3 after FFT along t_2. Rephasing, non-rephasing and scattering contributions oscillate along t_2 with frequency close to 0 or to the exciting laser frequency. The only Feynman paths oscillating at about twice the excitation frequency with the right phase matching condition and thus contributing to the 2Q signal are shown in panel (d). On the left the positive contribution (peak at $\omega_2 = E_{1,2}$ and $\omega_3 = E_1$) while on the right the negative one (peak at $\omega_2 = E_{1,2}$ and $\omega_3 = E_{1,2} - E_1 = E_2$).

$\omega_n \neq 0$ represent oscillating components associated to coherent dynamics along t_2. The corresponding amplitude a_n plotted in a 2D map as a function of ω_1 and ω_3 builds the so called DAS (dcay associated spectra) and CAS (coherence associated spectra), respectively. These maps allow the direct visualization of the sign and the amplitude distribution of a particular decay component along the 2D spectra. Given the n-th component associated to the time constant τ_n, a positive amplitude (yellow areas) will be found at positions in the 2D maps where the signal is decaying with τ_n, whereas a negative amplitude (blue areas) will be found where the signal is rising with τ_n.

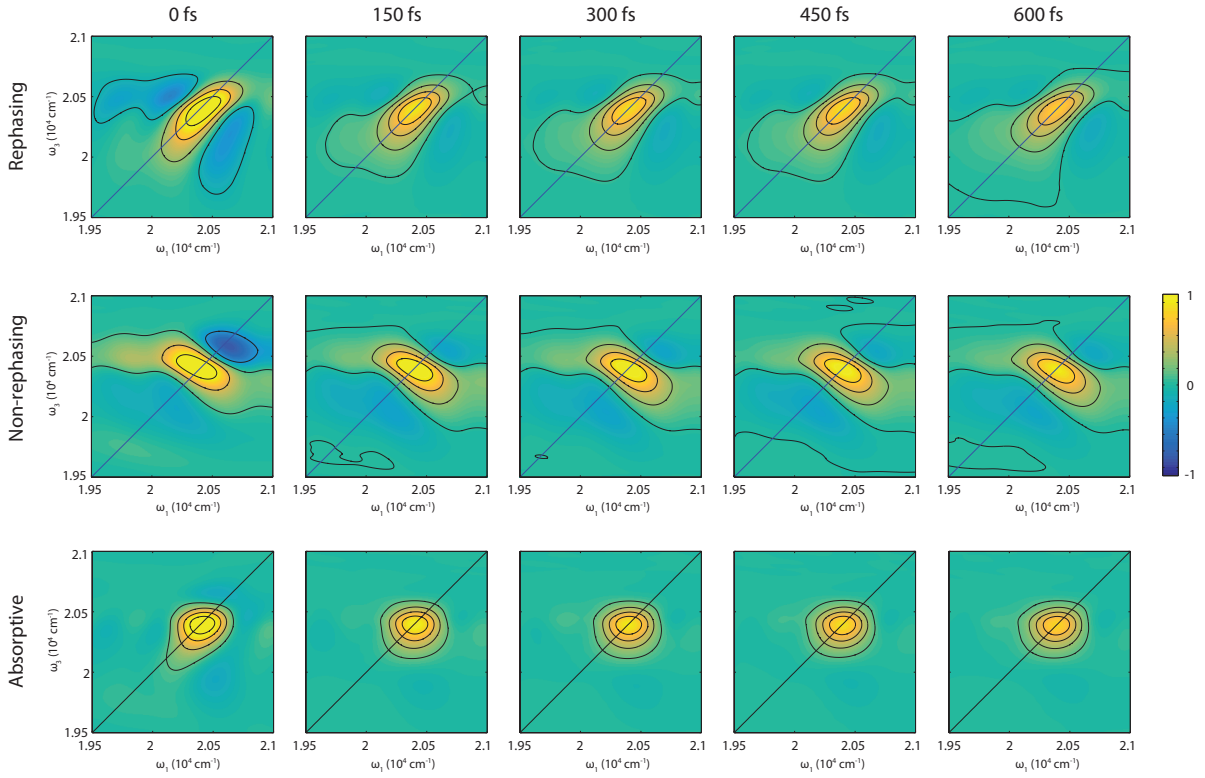

Figure S5: Real rephasing, non rephasing and purely absorptive spectra at selected values of t_2. All the spectra are normalized to their maximum.

The global fit of the R and NR complex signals recorded for the solution of H_2TPPS aggregate allowed the identification of 5 components, two associated with population decay and three with oscillating components, as reported in Table 1 of the main text. The DAS associated with the population decay constants are reported in figure S6. The CAS associated with oscillating components are reported in figure S7 and S8. In the R signal, CAS 1 and CAS 2 show the typical amplitude distribution expected for vibrational coherences, mainly localized in the region below diagonal. CAS 3 instead is characterized by a symmetrical distribution with respect to the diagonal, in agreement with the attribution of this CAS to a coherence having a mainly electronic character. The CAS of the NR signal are noisier and their interpretation is more difficult. In figure S7, the CAS obtained with our global fitting methodology are compared with the conventional Fourier maps (Turner D.B. et al. *J. Chem. Phys.* **2016**, 131, 144510); H.Li,et al. *Nat. Commun.* **2013** 4, 1390; J. O. Tollerud, et al.

Phys. Rev. Lett. **2016**, 117(9), 097401). In figure S8 we compare the CAS obtained from the analysis of experimental and simulated rephasing signal. In figure S7 and S8 colored dots indicate relevant positions where vibrational (red) and electronic (green) coherences are expected to contribute based on the simplified Displaced Harmonic Oscillators model (Turner D.B. et al. *Phys. Chem. Chem. Phys.* **2012**, 14, 4857). This model is not fully meaningful in our system for which a more advanced vibronic model is employed, but the pinpointed positions represent a guide for the eye and a support for the beating interpretation.

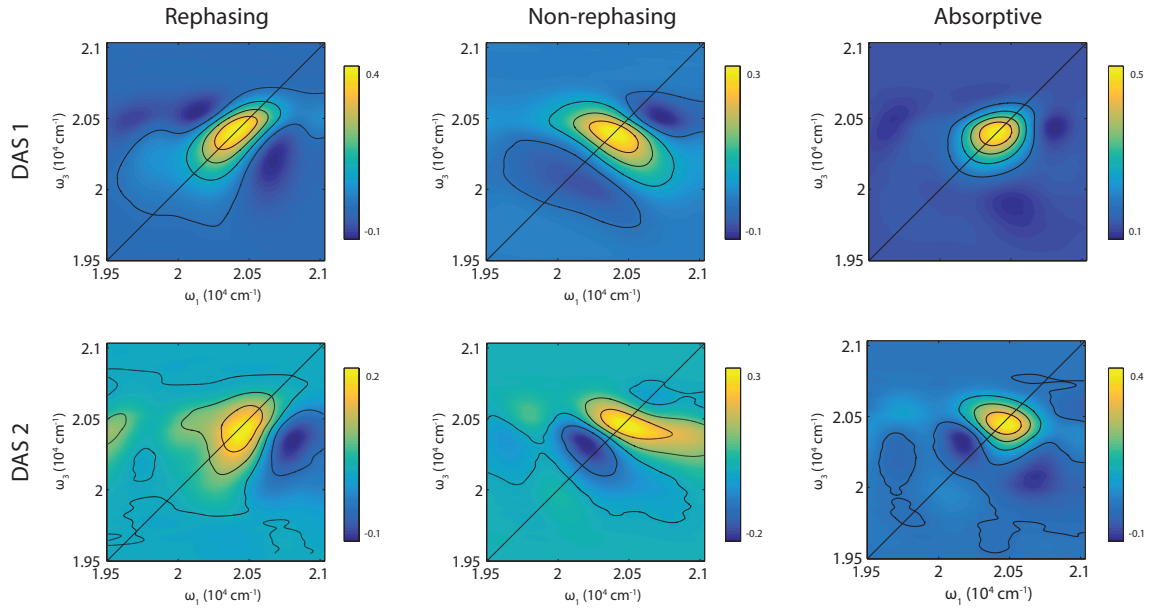

Figure S6: DAS of rephasing and non-rephasing signals. DAS 1 is associated to a time constant >1 ps and represents the global decay of R and NR maps during the whole investigated time-window. DAS 2 is associated to a faster time constant (280 fs) which was attributed to the intra-band relaxation toward lower energy states. The purely absorptive DAS on the right correspond to the sum of R and NR contributions.

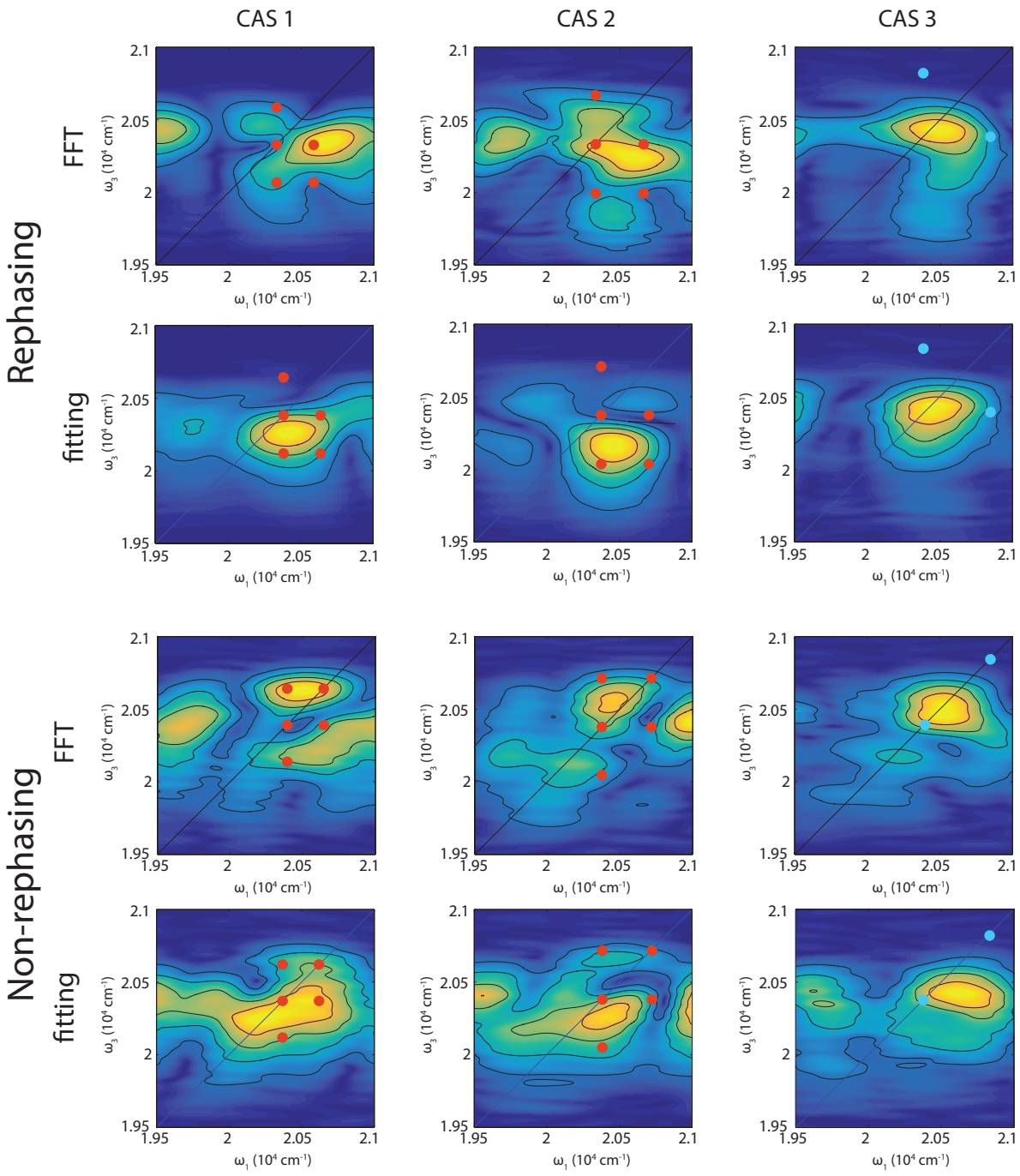

Figure S7: Comparison between the results of global fitting analysis (in terms of CAS) and conventional Fourier transform maps analysis of the oscillations in rephasing (upper panel) and non-rephasing (lower panel) contributions. The lower line in each panel reports the absolute CAS of the oscillating components of the signals. CAS 1,2 and 3 are associated to the 258, 334 and 445 cm^{-1} frequencies with dephasing times >1 ps, >1ps and 265 fs, respectively. The upper line in each panel reports the Fourier maps at corresponding frequencies. No information about dephasing times can be estimated in this case since FT maps describe the average behavior along the whole t_2 window investigated.

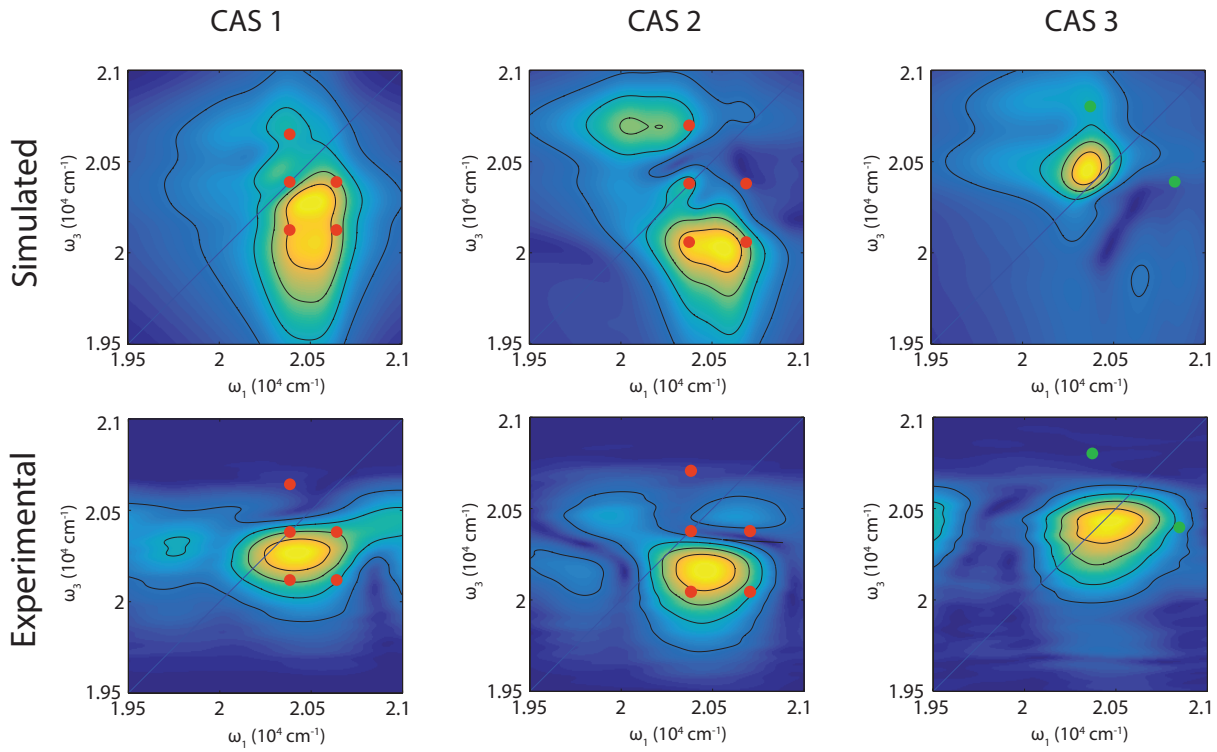

Figure S8: Comparison between simulated and experimental CAS of rephasing signal. In general, the shape of the simulated maps appear more elongated with respect of the experimental ones but still similar. This discrepancy is probably due to laser spectrum issues.